RESEARCH ARTICLE

Sustainability

Energy & Environmental Materials WILEY

"Win-Win" Structural Engineering of Chinese Herb Residues-Derived Porous Graphitic Carbons: Decoupling the Porosity-Graphitization Antagonism for Ultrahigh-Rate Supercapacitors

*Chuixiong Kong, Tingmin Di, Geming Wang, Quanrong Deng, Yuan Gao, and Shenggao Wang**

The antagonism between porosity and graphitization critically limits carbon supercapacitor performance. Here, we demonstrate a structural engineering strategy that converts Sargentodoxa Cuneata residue (SCR) into hierarchically porous graphitic carbons (SCR-HPCs). By precisely regulating biomass precursor porous architecture, this methodology decouples the antagonism between porosity development and graphitization progression in KOH-mediated activation, achieving simultaneous high specific surface area (2465.1 $m^2 g^{-1}$) and graphitization (I_D/I_G of 0.73). In 6 M KOH electrolyte, the specific capacitance of the optimized SCR-HPC-900 electrode reaches 415.6 $F g^{-1}$ at 0.5 A g^{-1}, with a capacitance retention of 75.1% even at an ultra-high current density of 200 A g^{-1}. The fabricated symmetric supercapacitor achieves an energy density of 8.5 Wh kg^{-1} at a power density of 37 803 W kg^{-1}, retaining over 100.8% of its capacitance after 100 000 cycles. Remarkably, in 1 M $TEABF_4$/PC organic electrolyte, the supercapacitor achieves maximum energy and power densities of 45.6 Wh kg^{-1} and 41 750 W kg^{-1}, respectively. This study presents an effective methodology for decoupling the antagonism between porosity and graphitization in conventional processes, offering a new idea for converting biomass waste into high-performance energy storage materials.

1. Introduction

Electric double-layer capacitors (EDLCs), serving as critical components in high-power electrochemical energy storage systems, derive their charge storage dynamics from electric double-layer capacitive behavior at electrode–electrolyte interfaces. Owing to millisecond-level charge/discharge response, exceptional cycling stability exceeding 10 000 cycles, and broad temperature adaptability, this technology demonstrates irreplaceable advantages in dynamic energy management scenarios including grid frequency regulation and rail transit regenerative braking systems.[1–5] Porous carbon materials, serving as the core energy storage medium, exhibit exceptional energy storage performance due to their porosity and high conductivity.[6–11] Yet, the antagonism between porosity and graphitization in carbon-based electrodes hinders performance optimization.[9,12,13] Therefore, developing carbon materials with both high specific surface area (SSA) and graphitization degree, while elucidating the intrinsic synergistic mechanisms between porous structure optimization and graphitization enhancement, holds crucial significance.

Biomass waste, such as agricultural and forestry wastes, food processing by-products, and traditional Chinese medicine residues, etc., is an ideal precursor for constructing porous carbons.[12,14–19] In recent years, there have been significant advancements in the research of converting biomass waste into porous graphitic carbon. Notably, the combined use of activators and graphitization catalysts, as well as the application of bi-functional catalysts (such as K_2FeO_4, $K_4Fe(CN)_6$, $K_3[Fe(C_2O_4)_3]$) that simultaneously achieve activation and graphitization, has been particularly prominent.[12]

For instance, Li et al.[20] demonstrated a method combining KOH activation with bimetallic Ni/Mo catalytic graphitization to convert wood shavings into porous graphitic carbon (PGC–Ni–Mo). The optimized material showed a 9.4% increase in graphitic crystallinity, achieved a specific capacitance of 267 $F g^{-1}$ at 1 A g^{-1}, retained 77.2% at 10 A g^{-1} (34.7% improvement), highlighting the synergistic effect of bimetal catalysis. Gong et al.[21] optimized the K_2FeO_4 activation process to simultaneously carbonize and graphitize bamboo charcoal (PGBC), producing PGBC electrode material with a high SSA (1732 $m^2 g^{-1}$) and excellent graphitization ($I_G/I_D = 1.61$), which showed a specific capacitance of 296.0 $F g^{-1}$ at 0.5 A g^{-1} in

Dr. C. Kong, Prof. T. Di, Prof. G. Wang, Prof. Q. Deng, Dr. Y. Gao, Prof. S. Wang
Provincial Key Laboratory of Plasma Chemistry and Advanced Materials, School of Materials Science and Engineering, Wuhan Institute of Technology, Wuhan 430205, China
E-mail: wyysg@wit.edu.cn
Dr. C. Kong
Department of Intelligent Manufacturing and Equipment, GuiZhou Vocational Technology College of Electronics & Information, Kaili 556000, China
The ORCID identification number(s) for the author(s) of this article can be found under https://doi.org/10.1002/eem2.70174.

DOI: 10.1002/eem2.70174

© 2025 The Author(s). *Energy & Environmental Materials* published by John Wiley & Sons Australia, Ltd on behalf of Zhengzhou University. This is an open access article under the terms of the Creative Commons Attribution License, which permits use, distribution and reproduction in any medium, provided the original work is properly cited.

6 M KOH electrolyte. Wu et al.[15] synthesized nitrogen/sulfur co-doped hierarchical porous carbon (NSHPC) using a dual-activation strategy. They employed Chinese rice wine lees as a carbon precursor, KOH as a chemical activator, and $FeCl_3 \cdot 6H_2O$ as a dual-functional catalyst/activator. The optimized NSHPC-700 has a SSA of 1357 $m^2 g^{-1}$ and graphitic ordering ($I_G/I_D = 1.05$), achieving 433.5 F g^{-1} at 1 A g^{-1} in 6 M KOH electrolyte.

Nevertheless, the current methods of preparation are constrained by high cost, complex procedures, and environmental incompatibility. Crucially, it is difficult to achieve both a well-developed porous structure and a high degree of graphitization with existing techniques. Since enhancing porosity often sacrifices the degree of graphitization and vice versa, this mutual restriction impedes the improvement of the overall performance of the material.[12] Moreover, regarding biomass-derived porous graphitic carbon, existing research primarily focuses on selecting precursor and activator species. However, to the best of our knowledge, there are few studies on synergistically optimizing the porosity and graphitization of porous carbon by regulating the pore structure of bio-carbon matrices.

Herein, the present work innovatively employs the medicinal plant Sargentodoxa cuneata (SC) as a precursor. During decoction, this material not only releases bioactive components but also spontaneously forms a natural interconnected pore network within its organic framework, exhibiting a unique self-templating effect, which offers a novel strategy for constructing carbon materials that combines high porosity with high graphitization. Compared to conventional biomass, SC requires no complex pretreatment or external templating agents, yet provides an ideal structural foundation for the KOH activation process, thereby effectively regulating the competition between pore structure development and graphitization. Inspired by these attributes, we propose a simple, efficient, and environmentally friendly "win-win" strategy that leverages the unique self-templating properties of SC to synergistically optimize the porous structure and graphitization of carbon materials during KOH activation. Ultimately, this approach enables the targeted conversion of its decoction residue (SCR) into high-performance hierarchical porous graphitic carbon (SCR-HPCs). An in-depth investigation was conducted to explore the influence of the porosity of biomass chars on the SSA, pore structure, and degree of graphitization of the as-derived porous carbon. The mechanism of KOH-induced graphitization was revealed by regulating the activation temperature. Structural characterization and electrochemical performance measurements demonstrated that constructing interconnected pore networks within the biomass char matrix facilitates homogeneous diffusion and mass transfer of the activator, eliminates the concentration gradient, and achieves synergistic optimization of the porosity and graphitization of the porous carbon. By optimizing the reaction conditions, the prepared porous graphitic carbon materials possessed high SSA, hierarchical porous architecture, and high degree of graphitization, resulting in superior electrochemical performance.

2. Results and Discussion

The hierarchical porous carbons (SC-HPCs and SCR-HPCs) were synthesized using SC and its decoction residue (SCR) as precursors via a combined pre-carbonization and KOH activation strategy (**Figure 1a**). SC, as a typical medicinal herb, possesses a lignocellulosic matrix (-cellulose/hemicellulose/lignin complex) with a high content of organic active ingredients (tannins, polyphenols, saponins, etc.[22]) that results in a distinctive biomass texture. Decoction pretreatment has been demonstrated to induce cell wall rupture and the release of active ingredients through a concentration gradient mass transfer effect, as well as to promote the decomposition of the lignin–carbohydrate complex (LCC).[23–25] This process establishes critical structural templates that facilitate the oriented growth of graphitic crystallites and the construction of a hierarchical porous structure during subsequent activation.

Scanning Electron Microscopy (SEM) images (Figure 1b–e) clearly reveal that both SC and SCR exhibit the raw SC unique 3D honeycomb-like porous structure, indicating their natural porosity. However, following decoction pretreatment, a significant change in the microstructure of the SCR was observed, with surface tissues separating to form a more loose skeletal structure (see Figure S1a,b, Supporting Information for cross-sections). Energy Dispersive Spectroscopy (EDS) verifies that the SC and SCR surfaces are mainly composed of carbon (C), oxygen (O), and nitrogen (N) (Figure 1f,g). The pore structure of SC and SCR was further investigated using N_2 adsorption/desorption at 77 K. As shown in Figure 1h,i, the decoction pretreatment raises the SSA from 12.3 $m^2 g^{-1}$ (SC) to 28.8 $m^2 g^{-1}$ (SCR), and increases mesopore numbers in the 2.4–8 nm range, demonstrating effective SSA and porosity optimization in SCR. Fourier transform infrared spectroscopy (FT-IR) analysis (Figure S2a–c, Supporting Information) reveals the distinct chemical structures of lignin, cellulose, and hemicellulose in both the SC and SCR samples.[26] Decoction pretreatment resulted in partial bond scission and reorganization of the cellulose and hemicellulose in the samples.[27] Also, the lignin aromatic ring conjugation system was partially disrupted and the hydroxyl hydrogen-bonding network was weakened.[14] The effect of decoction pretreatment on the chemical composition and bonding configuration of the SC surface was further evaluated by using X-ray Photoelectron Spectroscopy (XPS) spectroscopy (Figure S3, Supporting Information). As evidenced by the XPS analyses in Figure 1j–m and Table S1, Supporting Information, a notable decrease in sp^2-C content from 14.06% (SC) to 9.66% (SCR) was observed, indicating partial degradation of aromatic structures during pretreatment processing. Concurrently, the decrease in C–O content, combined with the increase in C=O and sp^3-C, suggests the oxidative transformation of ether and hydroxyl groups into aldehyde/carboxyl groups.[14] These findings offer direct proof of the chemical composition changes after decoction pretreatment. Overall, decoction effectively disrupts SC's original structure, forming a hierarchical porous framework that provides the structural foundation for the synthesis of high SSA porous graphitic carbon.

As illustrated in **Figure 2a**, the surface elemental composition of the porous carbon material was characterized using XPS. The quantitative analysis results (Table S2, Supporting Information) show that the C, O, and N contents of SC-BC and SCR-BC are 88.29%, 0.81%, 10.91% and 86.76%, 1.45%, 11.79%, respectively. The slightly higher content of heteroatoms in SCR-BC will provide a more reactive interface for its subsequent activation process.[28] It is noteworthy that oxygen content decreases significantly with increasing activation temperature in both groups of samples, but the decrease is more pronounced for the SCR-HPCs. These changes collectively optimize the energy storage performance by balancing increased surface area and conductivity against the reduced pseudocapacitance from oxygen functionalities.[29] The high-resolution O 1s XPS spectra (Figure 2b) reveal diverse oxygen binding states, including C=O (531.6 eV), C–O–C/C–OH (532.8 eV), and O=CO (534.1 eV).[30,31] As shown in Table S1, Supporting Information, the C=O contents of SC-BC and SCR-BC are 60.95% and 70.30%, respectively, indicating a greater surface activity of SCR-BC. The high-resolution C 1s XPS spectra (Figure 2c) were deconvoluted into four peaks centered at 283.2, 284.8, 286.6, and 289.0 eV, which

© 2025 The Author(s). *Energy & Environmental Materials* published by John Wiley & Sons Australia, Ltd on behalf of Zhengzhou University.

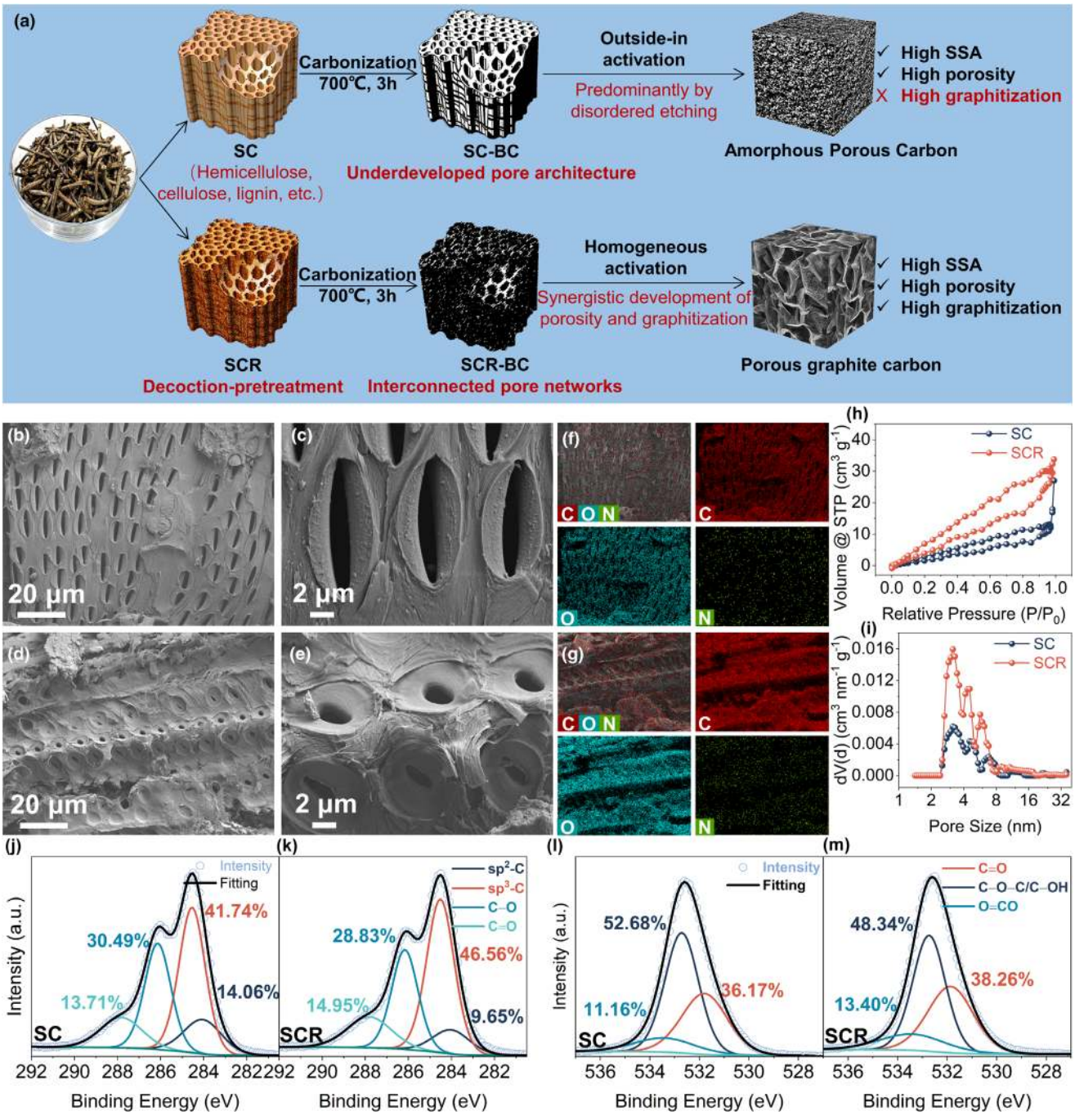


Figure 1. a) Schematic of the preparation of SC-HPCs and SCR-HPCs, b–e) SEM images, f, g) EDS mappings of C, O, and N, h) N_2 adsorption–desorption isotherms, i) pore size distribution, j, k) high-resolution XPS spectra of C 1s, and l, m) high-resolution XPS spectra of O 1s of SC and SCR samples.

are assigned to sp^2-C (C=C), sp^3-C (C–C), C–O, and C=O bonds, respectively.[32] Quantitative analysis demonstrates a negative correlation between the sp^3/sp^2 hybrid carbon ratio and the activation temperature of the porous carbon, confirming that high-temperature activation promotes the graphitized assembly of the carbon matrix.[33] The results indicate that the decoction pretreatment, by modifying the chemical state of precursors and increasing the activation reaction interface, effectively facilitates the conversion of sp^3 to sp^2 hybridization and significantly improves the ordering of the carbon skeleton.

As depicted in Figure 2d,g, the SCR-BC (SSA of 300.8 $m^2 g^{-1}$, V_{Tol} of 0.27 $cm^3 g^{-1}$) has a larger SSA and more favorable pore characteristics compared to SC-BC (SSA of 147.9 $m^2 g^{-1}$, V_{Tol} of 0.16 $cm^3 g^{-1}$). The results demonstrate that the decoction pretreatment successfully constructed a hierarchical porous structure with synergistic development of micro- and mesopores within the carbon matrix, which facilitates the homogeneous diffusion and mass transfer of the KOH. The higher diffusion coefficient ($D = 1.91 \times 10^{-12}$ $cm^2 s^{-1}$, Figure S4 and Table S3, Supporting Information) and more homogeneous distribution

© 2025 The Author(s). *Energy & Environmental Materials* published by John Wiley & Sons Australia, Ltd on behalf of Zhengzhou University.

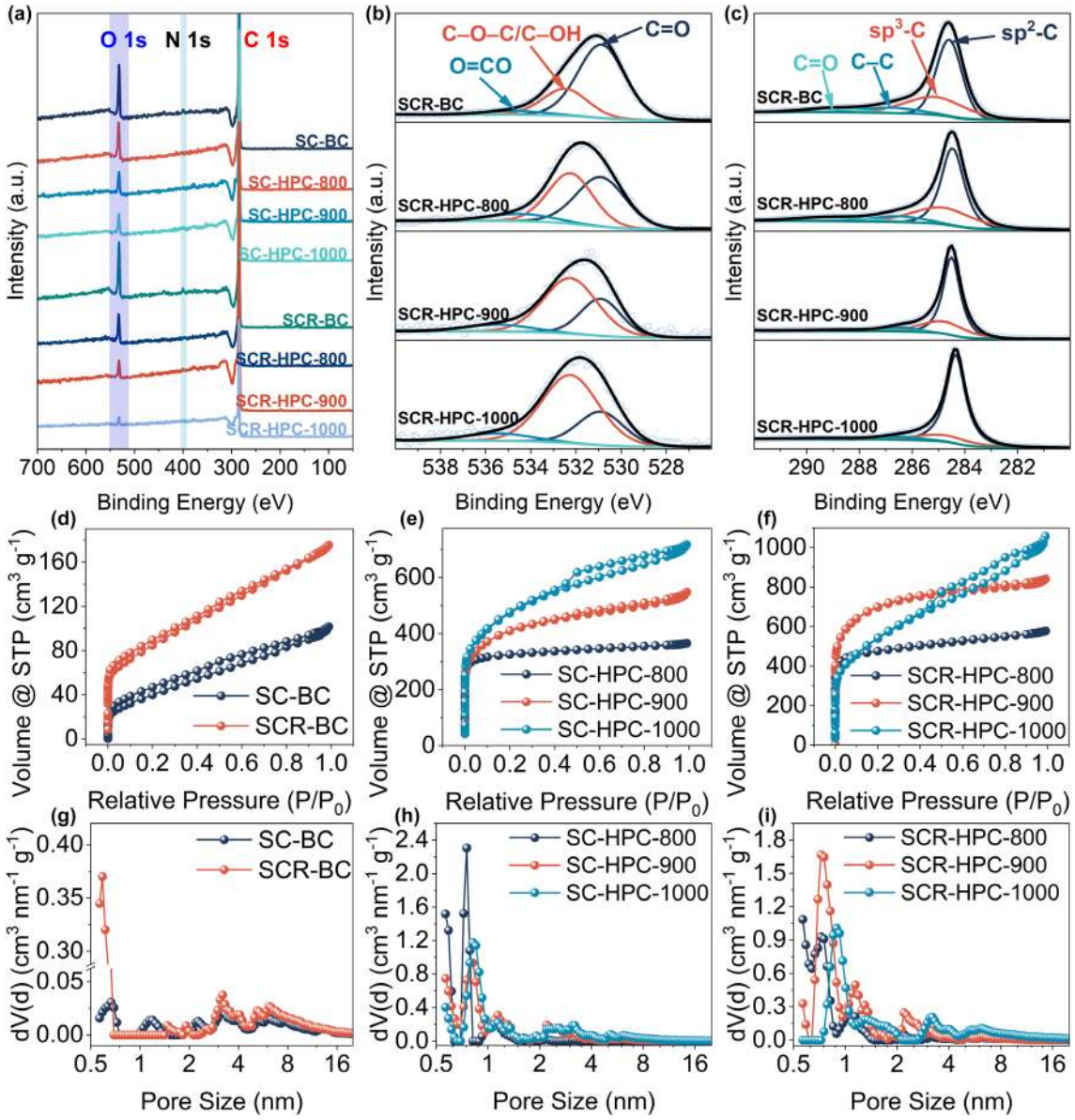


Figure 2. XPS and porosity characterization of SC- and SCR-derived porous carbon: a) XPS survey spectra, b, c) XPS spectra of O 1s and C 1s for SCR-BC and SCR-HPCs, d–f) nitrogen adsorption–desorption isotherms, g–i) pore size distribution.

of K elements in SCR-BC (Figures S5 and S6, Supporting Information) further confirm its advantages in activator distribution and mass transport. The optimizing structure in SCR provides a foundation for synthesizing carbon materials with SSA and a hierarchically porous structure. This has been verified in experiments carried out at different activation temperatures. As shown in Figure 2e,f, as the activation temperature rises, the isotherm shifts gradually from a Type I to a Type IV pattern with a pronounced H_3-type hysteresis loop at medium-to-high relative pressures ($P/P_0 > 0.4$), signifying a hierarchical porous structure with coexisting micropores and mesopores as well as enhanced pore connectivity.[34,35] Notably, under identical activation temperatures, SCR-HPCs consistently exhibit higher N_2 adsorption quantities than SC-HPCs, demonstrating that pretreatment effectively enhances the SSA and V_{Tol} of porous carbons. SC-HPCs (800–1000 °C) exhibit SSAs of 1281.9–1672.6 $m^2 g^{-1}$, whereas SCR-HPCs show significantly higher values (1843.7–2465.1 $m^2 g^{-1}$), highlighting the critical role of pretreatment in porosity optimization (see Table S4, Supporting Information for details). However, it has been demonstrated that excessive activation temperatures lead to a high degree of graphitization and partial structural collapse, which reduces the SSA of carbon materials, as evidenced in SCR-HPC-1000.

The PSD (Figure 2h,i) and pore structure parameters (Table S4, Supporting Information) demonstrate that all samples exhibit a predominant pore size distribution within the range of 0.5–2 nm. Notably, the pretreatment process significantly optimizes the pore architecture of SCR-HPCs. SCR-HPC-800 shows a 38% increase in micropore volume (0.62 $cm^3 g^{-1}$) and a remarkable 125% surge in mesopore volume (0.27 $cm^3 g^{-1}$) compared to SC-HPC-800. The optimal equilibrium of

© 2025 The Author(s). *Energy & Environmental Materials* published by John Wiley & Sons Australia, Ltd on behalf of Zhengzhou University.

this pore structure modulation effect is achieved at 900 °C. SCR-HPC-900 exhibits good pore structure characteristics, with a V_{Tol} of 1.27 $cm^3 g^{-1}$, a microporous volume fraction of 70.1%, a high SSA (2465.1 $m^2 g^{-1}$), and interconnected mesoporous channels (fraction of 29.9%). These features demonstrate the effectiveness of the pretreatment in synchronously optimizing both pore volume and size distribution. Micropores provide abundant active sites for electrolyte interaction, whereas mesopores facilitate ion transport by forming a loose diffusion layer, which reduces internal resistance and shortens diffusion pathways. Additionally, macropores act as electrolyte reservoirs and improve interfacial wetting, effectively reducing the resistance of ion transport and improving mass transfer efficiency.[36] Therefore, porous carbon with a suitable distribution of micropores and mesopores shows better electrochemical performance.[18]

SEM images reveal the microstructural evolution of SC- and SCR-derived porous carbon. As shown in **Figure 3**a,b, both the SC-BC and the SCR-BC have inherited the distinctive 3D architecture of the raw SC. However, their dense surfaces and underdeveloped porosity also reveal the structural limitations inherent to conventional pyrolysis processes. Thermal activation experiments have demonstrated a competitive mechanism of pore formation and graphitization in the evolution of the carbon skeleton. At 800 °C, both SC-HPC-800 and SCR-HPC-800 exhibit amorphous porous carbon matrices (Figure 3c,d). Thermal activation at 900 °C triggers structural reorganization, evidenced by the emergence of crumpled graphene nanoribbons on their surfaces (Figure 3e,f). Upon reaching 1000 °C, the materials undergo further graphitization, forming extended graphene nanoribbons with pronounced structural ordering (Figure 3g,h). These highly ordered graphene nanoribbons have the potential to enhance the overall electrochemical performance by facilitating electron transport, reducing internal resistance, and enhancing structural stability.[12,19,35] The results indicate that the microstructural evolution of the carbon materials exhibits significant temperature-dependent features, reflecting the dynamic competition between the development of porous architecture and the growth of graphite microcrystals: disordered KOH etching dominates the low-temperature activation process, forming an amorphous porous network, while ordered graphitization progressively prevails as the temperature rises.

Further analysis reveals that the pretreatment significantly influences the microstructure of porous carbon. As shown in Figure 3d, SCR-HPCs exhibit a well-developed pore architecture at 800 °C activation. At 900 °C, the SCR-HPCs exhibit a continuous distribution of wrinkled graphene nanoribbons, forming a distinctive soft–hard carbon composite structure (Figure 3f). A large number of channels and voids form between adjacent wrinkled graphene nanoribbons, providing a favorable environment for electron transport and ion diffusion.[37,38] In contrast, the surface of SC-HPC-900 retains an amorphous carbon matrix, with graphene nanoribbons confined to

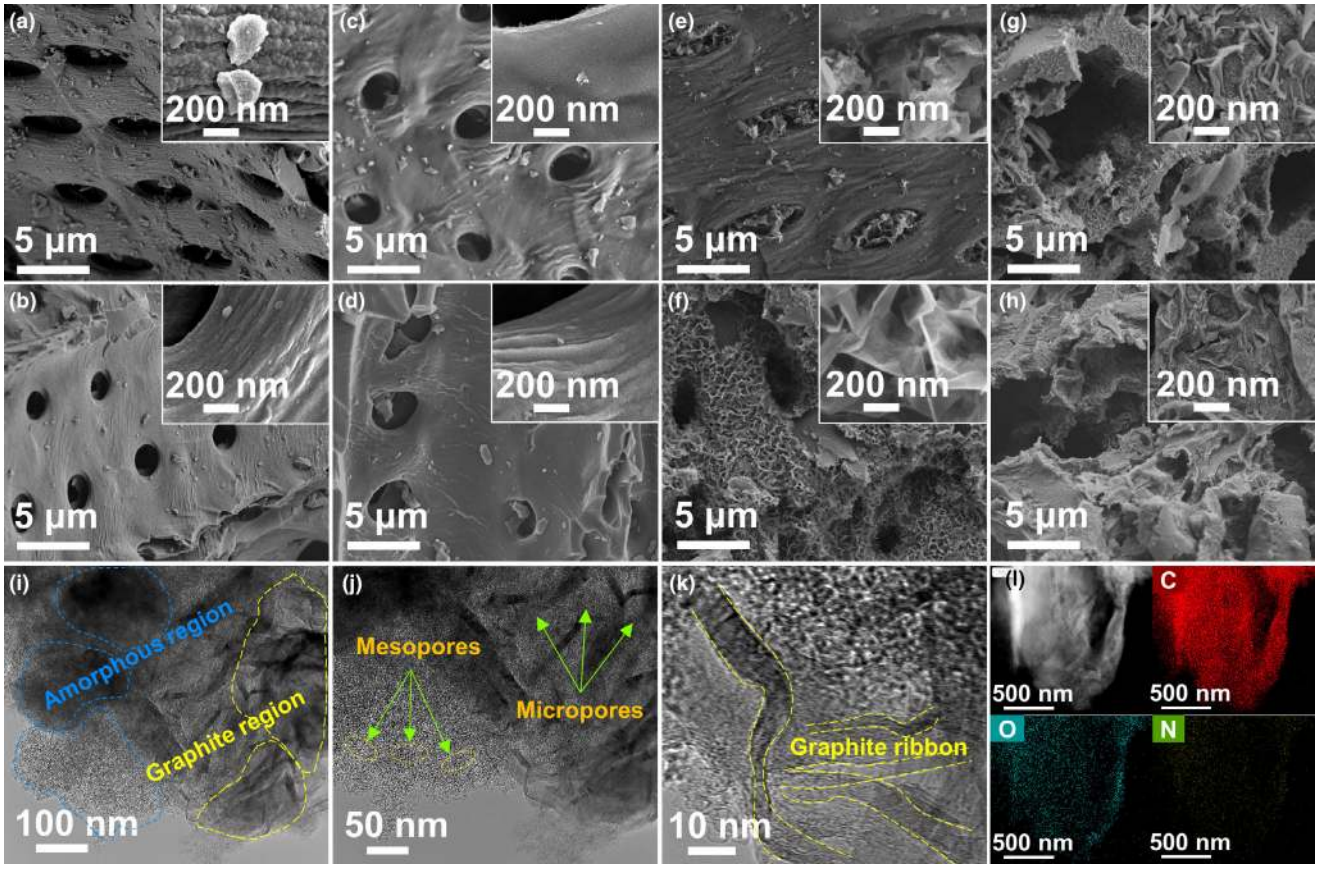


Figure 3. Surface morphologies and microstructures of SC- and SCR-derived porous carbon: SEM images of a) SC-BC, b) SCR-BC, c) SC-HPC-800, d) SCR-HPC-800, e) SC-HPC-900, f) SCR-HPC-900, g) SC-HPC-1000, h) SCR-HPC-1000, i–k) TEM images of SCR-HPC-900, and l) elemental mapping images of SCR-HPC-900.

© 2025 The Author(s). *Energy & Environmental Materials* published by John Wiley & Sons Australia, Ltd on behalf of Zhengzhou University.

macropores derived from the precursor (Figure 3e). Furthermore, SCR-HPC-1000 undergoes more intense graphite reorganization, yielding larger graphene nanoribbons (Figure 3h), while the wrinkled structure is significantly reduced. However, the SC-HPC-1000 exhibits a structure similar to the SC-HPC-900 (Figure 3g), but the graphene size appears to be smaller. TEM images further reveal the structural features of SCR-HHP-900. As shown in Figure 3i, the material exhibits a distinct hard–soft carbon composite topology, with both amorphous carbon regions and graphene nanoribbons clearly visible, which contributes to enhanced electrochemical charge storage and electrical conductivity. Figure 3j shows a highly developed hierarchical porous structure with noticeable micro- and mesopores. The HRTEM image (Figure 3k) reveals graphene nanoribbons with clear lattice fringes, indicating high crystallinity. Elemental mapping (Figure 3l) confirms the homogeneous distribution of oxygen and nitrogen within the carbon framework. Furthermore, the high-resolution TEM image of SCR-HPC-900 exhibits a well-defined diffraction pattern of a long-range ordered graphite lattice after Fourier transformation (Figure S7, Supporting Information). By measuring the lattice fringe spacing across 10 different regions, an average interlayer distance of $d_{002} = 0.3401$ nm was obtained, approaching that of ideal graphite (0.335 nm), with significant continuous crystalline domains observed. This value is in close agreement with the result calculated from X-ray diffraction (XRD) (0.342 nm).

The XRD patterns of porous carbons (**Figure 4**a,b) exhibit two characteristic peaks at ~22° and 44°, corresponding to the (002) and (100) planes of graphitic carbon.[14] As the activation temperature increased, the (002) diffraction peak of the activated samples (SC-HPCs and SCR-HPCs) gradually shifted to a higher angle and sharpened near 26° (Figure 4a,b), indicating not only an increase in sp^2 hybridized carbon domains but also a decrease in interlayer spacing (d_{002}), enhanced structural ordering, and increased crystallinity.[20] The XRD crystallite size analysis results (Table S5, Supporting Information) indicate that the degree of graphitization in the carbon material increases with rising activation temperature. Collectively, these changes contribute to the improved electrical conductivity and thermal stability of the carbon materials. In addition, the intensity of the diffraction peak at 26° for SCR-HPCs significantly enhances at activation temperatures higher than 900 °C. Raman spectroscopy was employed to further explore the effects of precursor structure engineering on the structural disorder–order evolution in porous carbon materials. As shown in Figure 4c,d, all samples exhibit two distinct characteristic peaks corresponding to the D band (~1340 cm^{-1}) and G band (~1590 cm^{-1}), respectively. Among them, SC-BC and SCR-BC show comparable structural disorder, with I_D/I_G intensity ratios of 0.89 and 0.88, respectively (Figure 4e,f). After activation, the SC-HPC-800 and SCR-HPC-800 exhibit I_D/I_G intensity ratios of 1.11 and 1.38, respectively, with minor 2D peaks emerging. At an activation temperature of 900°C, the I_D/I_G intensity ratio of SC-HPCs further increases to 1.14, indicating the continued accumulation of disordered defects. In contrast, the I_D/I_G ratio of the SCR-HPCs decreases to 0.73, suggesting that the pretreatment facilitates the ordered assembly of sp^2-C. Additionally, the I_{2D}/I_G ratio of SCR-HPC-900 is 0.50, which is significantly higher than that of SC-HPC-900 (0.31), consistent with its superior graphitization and crystallinity. For high-temperature activation, SCR-HPC-1000 exhibits a low I_D/I_G ratio of 0.36 and an increased I_{2D}/I_G ratio of 0.55, confirming enhanced graphitization. This result can be attributed to the synergistic interplay among preengineered carbon structure, high-temperature defect healing, potassium catalysis, and the decoupling of antagonism.[19,35]

The D bands in the Raman spectra were deconvoluted into four subbands using Gaussian-Lorentz numerical fitting (Figure 4g–n and Table S6, Supporting Information).[39] The results demonstrate that the intensity ratios of I_{D1}/I_G (reflecting defect concentration) and I_{D3}/I_G (representing the proportion of amorphous phases) first increase and then decrease with rising activation temperature, peaking at 800 °C for both SC-HPCs and SCR-HPCs.[40,41] Notably, the I_{D1}/I_G and I_{D3}/I_G ratios for SCR-HPCs decrease more rapidly at higher temperatures, indicating that precursor structural engineering accelerates the transformation of porous carbons from disorder to order. The I_{D2}/I_G intensity ratio also shows a clear temperature-dependent trend, increasing initially before declining beyond 900 °C. This nonmonotonic behavior reflects competing mechanisms during KOH activation: etching dominates at lower temperatures, introducing edge defects such as dislocations and dangling bonds that raise I_{D2}/I_G, while graphitization prevails at higher temperatures, promoting structural ordering and edge reorganization that reduce the ratio. Notably, SC-HPCs exhibit consistently higher I_{D2}/I_G values than SCR-HPCs across all temperatures, indicating that the pretreatment endows the precursor with more developed three-dimensional diffusion pathways and suppresses disordered defect formation through more uniform etching. Additionally, the intensity of the D4 band, which is associated with heteroatom-related defects, gradually decreased with increasing temperature, a trend consistent with the XPS analysis. Based on a statistical analysis of 152 porous carbon samples reported in the literature (Figure 4o and Table S7, Supporting Information),[10,15,17,18,20,21,26,30,32,33,41–67] the results show that 79.6% of the samples exhibit I_D/I_G ratios ranging from 0.8 to 1.2, with only 5.3% of the samples having ratios below 0.8. This indicates a significant antagonistic effect between porosity and graphitization in the structural development of porous carbon materials. In this study, the I_D/I_G ratios of SC-HPCs (1.11 at 800 °C, 1.17 at 900 °C, and 1.07 at 1000 °C) remain highly consistent with this statistical pattern. In contrast, the SCR-HPCs, which underwent decoction pretreatment, exhibit significant variations: the ratio rises to 1.38 at 800 °C (indicating more pronounced disordered etching), declines sharply to 0.73 at 900 °C (reflecting synergy between pore development and graphite microcrystal assembly), and falls further to 0.36 at 1000 °C (corresponding to the formation of long-range ordered graphitic domains), thereby systematically deviating from the statistical trend. Such a temperature gradient response feature reveals that pretreatment, through structural engineering of precursors, effectively decouples the kinetic competition between porosity formation and graphitization in conventional processes.

Based on the above experimental results, the formation mechanism of porous graphitic carbon can be rationally inferred. The KOH activation of carbon materials involves multiple mechanisms: 1) chemical etching by KOH and its derivatives (e.g., K_2CO_3 and K_2O) generates hierarchical porosity, 2) physical activation via gaseous products (CO_2 and H_2O) optimizes pore structure, and 3) catalytic graphitization through the intercalation of potassium into carbon lattices.[21,35] During activation, KOH preferentially reacts with sp^3-C and oxygen-containing groups in the carbon matrix and undergoes a disordered etching from the outside to the inside, which mainly produces K_2CO_3.[19,35] As etching proceeds, the sp^3-C and oxygen-containing functional groups in the carbon matrix are gradually consumed, resulting in an increase in the number of graphite microcrystals unconstrained by sp^3-C. This, in turn, provides a greater quantity of feedstock for the graphitization process. When the activation temperature exceeds the melting point of K_2CO_3 ($T_m = 891$ °C), the reaction changes from a solid–solid reaction

© 2025 The Author(s). *Energy & Environmental Materials* published by John Wiley & Sons Australia, Ltd on behalf of Zhengzhou University.

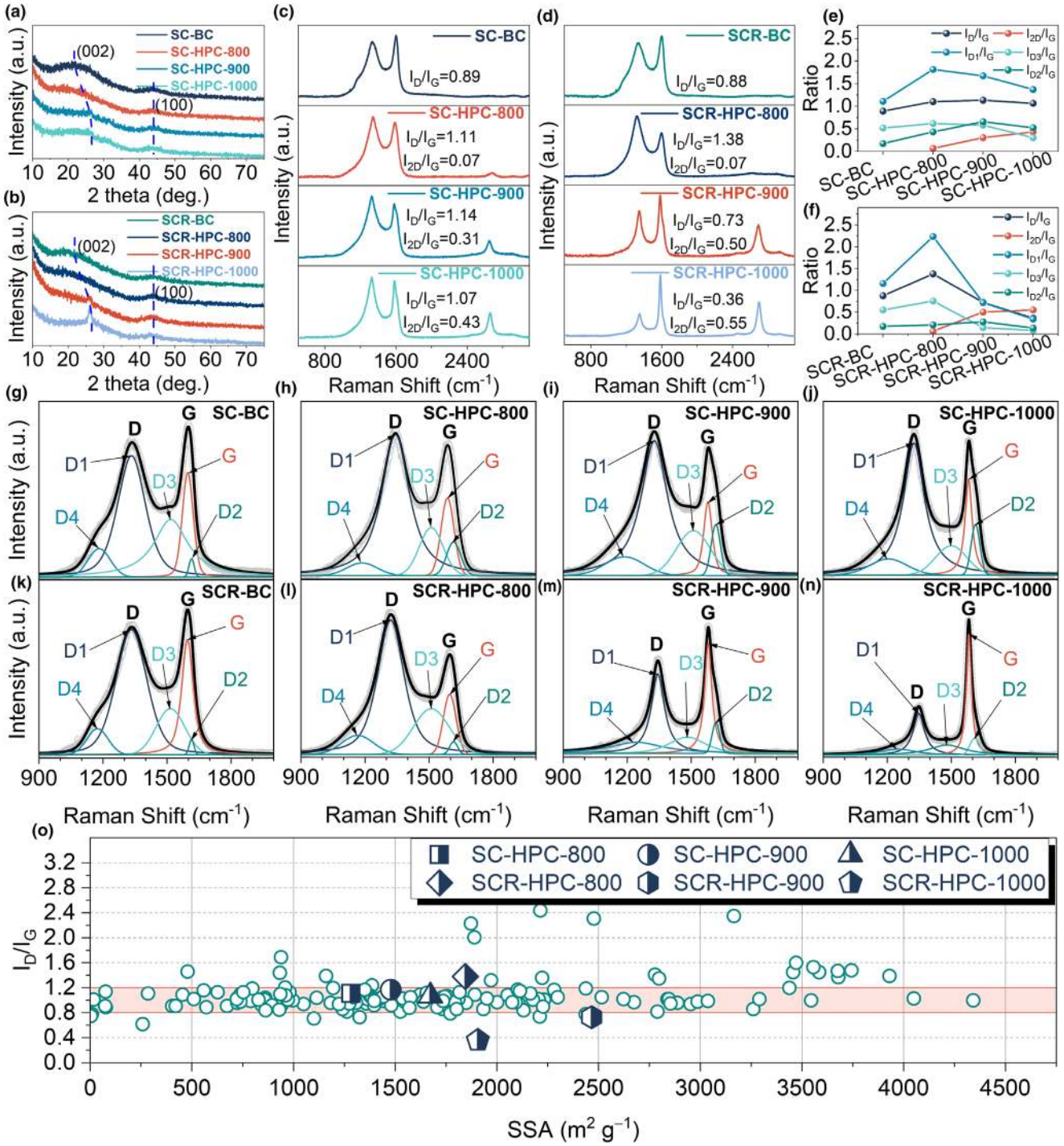


Figure 4. Structural characterizations of SC- and SCR-derived porous carbon: a, b) XRD patterns, c, d) Raman spectra, e, f) trend of I_D/I_G, I_{2D}/I_G, I_{D1}/I_G, I_{D2}/I_G, and I_{D3}/I_G values, g–n) Raman spectra with fitted curves, and o) I_D/I_G ratios as a function of the corresponding SSA of the reported porous carbon materials.

to a solid–liquid reaction. In situ XRD results (Figure S8, Supporting Information) indicate that the emergence of liquid-phase K_2CO_3 provides a key driving force for the formation of large graphene domains and accelerates the graphitization process.[20,27] In the case of SC-HPCs, the raw SC was carbonized at 700 °C to form a dense aromatic carbon skeleton with a relatively underdeveloped pore structure. In the presence of KOH, the lack of interconnected pores hinders the penetration of KOH into the interior, resulting in uneven activator distribution and predominantly disordered etching from the outside to the inside. At elevated temperatures, the carbon matrix is rapidly oxidized and etched by the high concentration of K_2CO_3 on the outer surface. This process disrupts the graphite microcrystal structure, thereby hindering

© 2025 The Author(s). *Energy & Environmental Materials* published by John Wiley & Sons Australia, Ltd on behalf of Zhengzhou University.

its potential to reorganize into graphene nanoribbons. Additionally, the disorder of the structure is further exacerbated by gases (e.g., CO_2 and H_2O) produced by violent reactions on the outer surface. Conversely, the etching effect of KOH within the internal macropores may be less pronounced, and graphite microcrystals have the opportunity to undergo ordered reorganization to form graphene nanoribbons. In the case of SCR-HPCs, the microstructure and chemical composition of the raw SC were changed by pretreatment, constructing a hierarchical porous structure enriched with reactive functional groups (sp^3–C, C=O, etc.) in the carbon matrix. Such a structure could provide abundant active sites and exposure interfaces for subsequent KOH activation. More importantly, the interconnected porous structure facilitates the uniform diffusion and reaction mass transport and eliminates the concentration gradient of the activator, achieving synergistic optimization of the porous structure development and graphitization, thereby creating favorable conditions for the storage and transfer of charges, which is expected to achieve a superior electrochemical energy storage.

The electrochemical performances of the as-prepared samples were characterized by a three-electrode system using 6 M KOH solution as the electrolyte. The cyclic voltammetry (CV) curves of SC-HPCs and SCR-HPCs at 50 mV s^{-1} are displayed in **Figure 5**a. The CV curves of all the samples exhibit rectangle-like curves without obvious redox peaks, demonstrating typical EDLC behavior.[68] Among them, SCR-HPC-900 shows the largest integrated CV area, indicating the highest specific capacitance, which results from its optimized hierarchical porous structure, high SSA (2465.1 m^2 g^{-1}) and appropriate degree of graphitization. The galvanostatic charge/discharge (GCD) curves of the SC-HPCs and the SCR-HPCs at 0.5–200 A g^{-1} are shown in Figure S9a–f, Supporting Information. The charge/discharge curves of all samples exhibit approximately triangular shapes, indicating good electrochemical reversibility. The specific capacitances of all electrodes, obtained

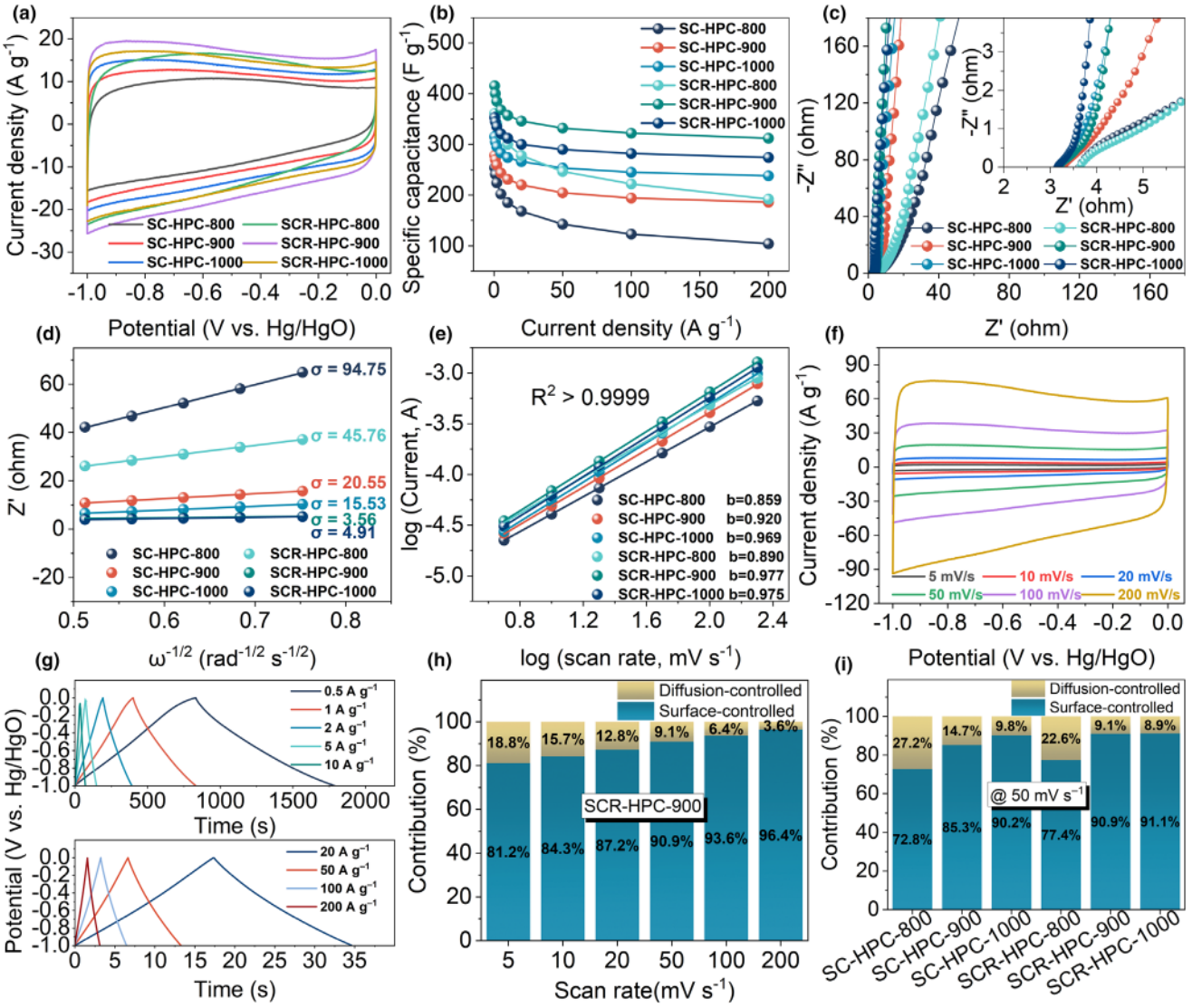


Figure 5. Electrochemical performances of SC-HPCs and SCR-HPCs at three-electrode: a) CV curves at 50 mV s^{-1}, b) rate performances, c) Nyquist plots, d) The linear relation of $\omega^{-1/2}$ versus Z′, e) absolute current density and scan rate follow the power law, $i = kv^b$, f–h) CV, GCD curves and capacitance contributions at different scan rates of SCR-HPC-900, respectively, i) the comparison of the capacitance contributions at 50 mV s^{-1}.

© 2025 The Author(s). *Energy & Environmental Materials* published by John Wiley & Sons Australia, Ltd on behalf of Zhengzhou University.

from galvanostatic charge–discharge (GCD) tests at various current densities, are shown in Figure 5b. At a current density of 0.5 A g^{-1}, the specific capacitances of the SC-HPC-800, SC-HPC-900, SC-HPC-1000, SCR-HPC-800, SCR-HPC-900, and SCR-HPC-1000 are 253.9, 278.3, 315.2, 361.2, 415.6, and 353.1 F g^{-1}. The SCR-HPC-900 exhibits the highest specific capacitance, approximately 1.5 times greater than that of the SC-HPC-900, which is consistent with the CV results. Clearly, SCR-HPCs electrodes have higher specific capacitance compared to SC-HPCs. As the current density increases to 200 A g^{-1}, the specific capacitance of all the electrodes decreases to some extent. The SC-HPCs electrodes exhibit a rate performance of 41.0%, 66.8%, and 75.5%, respectively, while the SCR-HPCs electrodes achieve 53.2%, 75.1%, and 77.6%. Obviously, demonstrating superior rate performance. The relatively lower rate performance of SC-HPC-800 and SCR-HPC-800 is primarily attributed to their micropores-dominated pore structure (which restricts rapid ion transport) and lower degree of graphitization (resulting in reduced electrical conductivity). Moreover, the optimized SCR-HPC-900 exhibits superior specific capacitance and rate performance relative to the most advanced carbonaceous electrodes in recently reported literature (Table S7, Supporting Information).

The Nyquist plots are depicted in Figure 5c. The curves are almost semicircle-free in the high-frequency region and nearly vertical in the low-frequency region (except for the samples activated at 800 °C), demonstrating rapid ion diffusion and ideal EDLC behavior. This can be attributed to the hierarchical porous structure and the suitable graphitization of the electrode material, which synergistically enhance the charge transfer and ion diffusion capability.[69] To gain insight into the ion diffusion process, the Warburg factor (σ), which represents the ion diffusion resistance, was calculated from the slope of the fitted curve by constructing a linear relationship between the impedance (Z') and the reciprocal of the square root of the angular frequency ($\omega^{-1/2}$) in the low-frequency region.[70] The synergistic effects of a well-developed hierarchical porous structure and suitable graphitization in SCR-HPC-900 substantially mitigate ion diffusion resistance and create abundant ion transport channels. This endows the SCR-HPC-900 electrode with the smallest Warburg coefficient ($\sigma = 3.56$, Figure 5d), markedly enhancing its electrochemical performance. The impedance spectra were fitted to equivalent circuits (Figure S10, Supporting Information) using ZView software, with the resulting R_s, R_{ct}, and R_w values listed in Table S8, Supporting Information. The R_w values for all samples (SC-/SCR-HPC-800/900/1000) range from 6.26 to 1.41 Ω and indicate a clear decreasing trend, which aligns closely with the variation of the Warburg coefficient (σ) in Figure 5d. Furthermore, the diffusion coefficients (D) in SC-HPCs and SCR-HPCs were investigated from follow equation:[71]

$$Z' = R_s + R_{ct} + \sigma\omega^{-1/2} \quad (1)$$

$$D = \frac{R^2T^2}{2A^2n^4C^2F^4\sigma^2} \quad (2)$$

where R, T, A, n, C, F, and σ represent the gas constant, absolute temperature (K), effective electrode area, electron transfer numbers, concentration of ions, Faraday constant, and Warburg coefficient, respectively. As summarized in Table S8, Supporting Information, the SCR-HPC-900 electrode shows a rapid D (1.55×10^{-7} cm^2 s^{-1}) compared to other electrodes. The result suggests that the diffusion kinetics of SCR-HPC-900 is enhanced significantly, which is attributed to the well-developed hierarchical porous structure that provides efficient pathways for ionic transport and a moderate degree of graphitization that ensures good electronic conductivity of the SCR-HPC-900.

The charge storage kinetic behavior of the SC-HPCs and SCR-HPCs was analyzed in depth by using CV curves (Figure 5f; Figure S11a–e, Supporting Information).[72] The power law relationship between the scan rate and current density is illustrated in Figure 5e. According to the Dunn kinetic model, the b value, as a characteristic parameter of the charge storage mechanism, presents a clear threshold response, where a b value of 0.5 implies that the current is controlled by a diffusion process, whereas a b value of 1.0 indicates that the current follows an ideal surface-controlled process.[73] The b value of the SCR-HPC-900 electrode was calculated to be 0.977, confirming ultrafast charge storage kinetics approaching that of an ideal electric double-layer capacitor. As depicted in Figure 5f, the SCR-HPC-900 electrode exhibits superior rate performance and ideal EDLC behavior over a wide range of scan rates (5–200 mV s^{-1}), and the CV curve maintains a quasirectangular feature at a high scan rate of 200 mV s^{-1}. Similarly, the GCD curve of the SCR-HPC-900 electrode exhibits a symmetric triangular shape without obvious IR drop even at an ultra-high current density of 200 A g^{-1} (Figure 5g), consistent with the results of the CV test.

Figure 5h depicts the results of the quantitative analysis of the surface-controlled versus diffusion-controlled contribution ratios for the SCR-HPC-900 electrode. A significant increase in the surface-controlled proportion from 81.2% to 96.4% was observed when the scan rate was increased from 5 to 200 mV s^{-1}. This phenomenon can be attributed to the kinetic limiting effect of diffusion-controlled processes under rapid scanning conditions, resulting in surface-controlled kinetic processes acting as the dominant mechanism for charge storage.[74] As displayed in Figure 5i, the charge storage of all electrodes is dominated by surface-controlled kinetics with minor diffusion-controlled contributions. Obviously, the surface-controlled contributions of the SCR-HPCs are higher than those of the SC-HPCs fabricated at the same temperature, and this gap is more pronounced at low activation temperatures. The results demonstrate that pretreatment significantly optimizes the ion/electron transport paths and charge transfer kinetics of the electrode materials, resulting in excellent rate performance.

To evaluate the performance of SCR-HPC-900 electrode in practical applications, symmetric supercapacitors SCR-HPC-900//SCR-HPC-900 were assembled by using 6 M KOH as electrolyte. As shown in **Figure 6**a, the CV curves of the capacitor at various scan rates (5–500 mV s^{-1}) maintain good quasirectangular features, reflecting the excellent rate performance and rapid charge response of the electrodes. Additionally, the CV curves (Figure S12, Supporting Information) measured at different operating potentials indicate that the devices exhibit a stability window extending up to 1.3 V.[75] The GCD curves are approximately symmetric triangles at different current densities (0.5–100 A g^{-1}), showing good EDLC behavior (Figure 6b). The EIS test results (Figure 6c) indicate that the capacitor has low equivalent series and charge-transfer resistances, rapid ionic diffusion kinetics (ion relaxation time $\tau_0 = 0.27$ s, Figure S13a, Supporting Information), and an ideal EDLC behavior, as evidenced by the small intercepts and semicircle diameter in the high- and mid-frequency regions, and a nearly vertical low-frequency curve. Based on these advantages, the capacitor exhibits excellent rate performance with a capacitance retention of 68.9% at 100 A g^{-1} (Figure S13b, Supporting Information). The Ragone plot of the SCR-HPC-900//SCR-HPC-900 is illustrated in Figure 6d. The energy density of the supercapacitor is 14.9 Wh kg^{-1} at

© 2025 The Author(s). *Energy & Environmental Materials* published by John Wiley & Sons Australia, Ltd on behalf of Zhengzhou University.

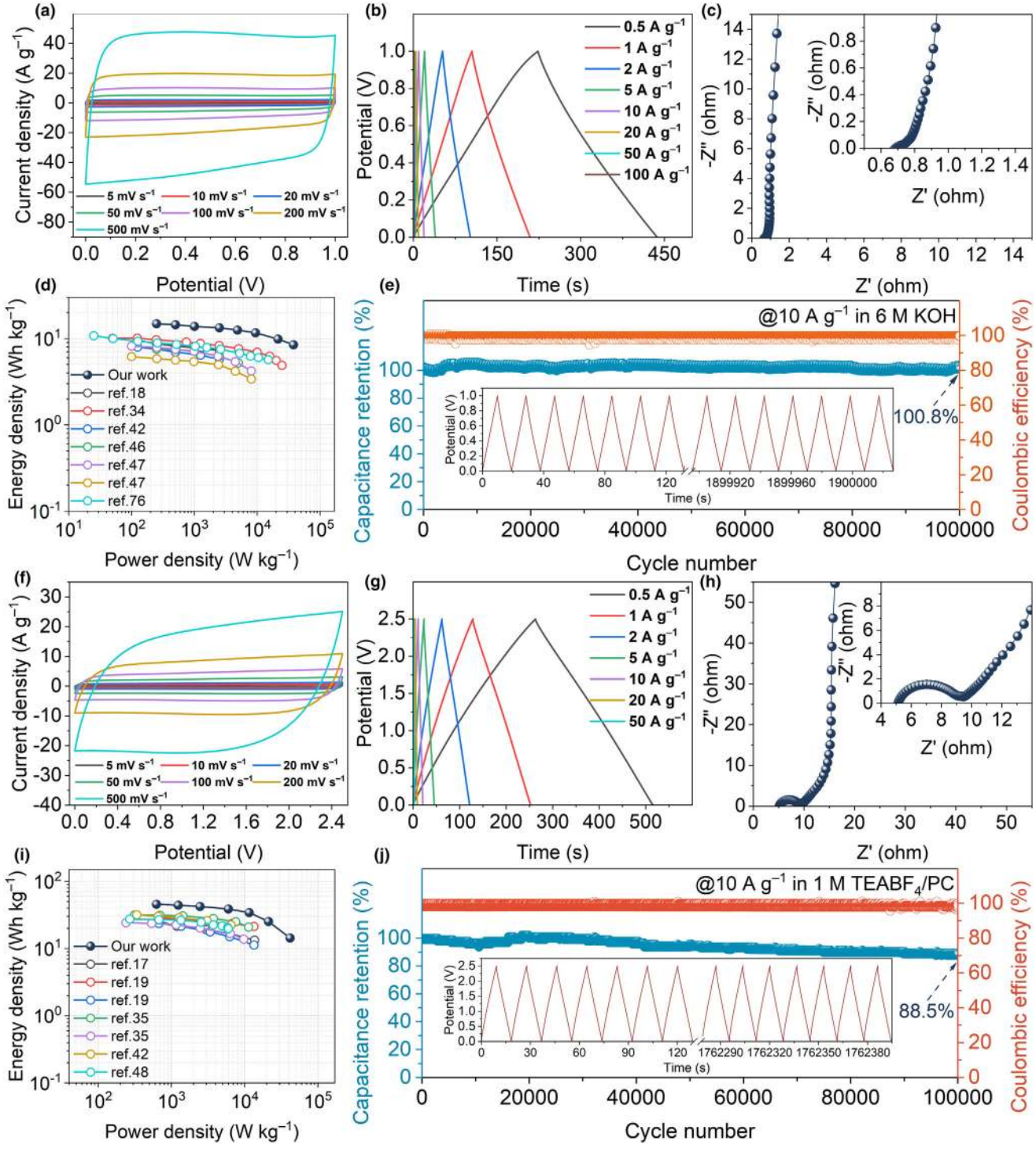


Figure 6. Electrochemical properties of SCR-HPC-900//SCR-HPC-900 symmetric supercapacitor in both 6 M KOH and 1 M $TEABF_4$/PC electrolytes: a) CV curves, b) GCD curves, c) Nyquist plots, d) Ragone plots, e) cycle performance in KOH electrolyte, f) CV curves, g) GCD curves, h) Nyquist plots, i) Ragone plots, j) cycle performance in $TEABF_4$/PC electrolyte. The electrode featured an active material mass loading of ~1.5 mg cm^{-2} and was fabricated from a slurry with a mass ratio of 8:1:1 (active material:acetylene black:PVDF) using NMP as the solvent.

a power density of 250 W kg^{-1}, and even at a high power density of 37,803 W kg^{-1}, the energy density can be maintained at 8.5 Wh kg^{-1}, which is superior to that of the porous carbon-based symmetric supercapacitors reported in the literature (Table S9, Supporting Information).[18,34,42,46,47,76] The cycling stability test results (Figure 6e) show that the SCR-HPC-900//SCR-HPC-900 has a

© 2025 The Author(s). *Energy & Environmental Materials* published by John Wiley & Sons Australia, Ltd on behalf of Zhengzhou University.

capacitance retention of 100.8% and a Coulombic efficiency over 99.8% after 100,000 cycles at 10 A g^{-1}. Furthermore, three series-connected SCR-HPC-900//SCR-HPC-900 successfully lit up an LED device (Figure S14, Supporting Information), further evidencing its excellent capacitance performance and practical application potential.

Since aqueous carbon-based supercapacitors usually have a narrow operating voltage window, to improve the practical applicability, the operating voltage window of the SCR-HPC-900//SCR-HPC-900 symmetric supercapacitor was further widened from 1.0 V with 6 M KOH electrolyte to 2.5 V by employing 1 M $TEABF_4$/PC electrolyte. As depicted in Figure 6f, the CV curves of the SCR-HPC-900//SCR-HPC-900 symmetric supercapacitor exhibit a quasirectangular feature at a scan rate of 500 mV s^{-1}, indicative of superior rate performance.[77] Additionally, the GCD curves exhibit nearly symmetric triangular shapes (Figure 6g), a feature that reflects good EDLC behavior. However, the larger ion radius of organic electrolytes increases transport resistance in porous electrodes compared to aqueous ones.[14] When comparing the Nyquist plot of an organic electrolyte system (Figure 6h) to that of an aqueous electrolyte (Figure 6c), it is observed that the former exhibits a smaller slope in the low-frequency region and a larger semicircle in the high-frequency region. This can be attributed to the larger radius of the organic electrolyte ions, which consequently leads to an increase in the transport resistance of ions within a porous electrode. Furthermore, the corresponding Bode plot (Figure S15a, Supporting Information) indicates a τ_0 of 2.17 s. To gain deeper insight into the ion diffusion kinetics, Electrochemical Impedance Spectroscopy (EIS) of SC-HPC-900 was additionally performed in a two-electrode system, as shown in Figure S16a,b, Supporting Information. The values of R_s, R_{ct}, and R_w obtained by fitting with the equivalent circuit (Figure S10, Supporting Information) are summarized in Table S10, Supporting Information. The results show that in 6 M KOH electrolyte, the R_w values of SC-HPC-900 and SCR-HPC-900 electrodes are 0.31 and 0.18 Ω, respectively, while in 1 M $TEABF_4$/PC electrolyte, the R_w values are 4.08 and 3.34 Ω, respectively. Evidently, in both electrolytes, the pretreatment significantly reduces the R_w of SCR-HPC-900. Additionally, EIS (Figure S16, Supporting Information) and Galvanostatic Intermittent Titration Technique (GITT) (Figure S17, Supporting Information) results demonstrate that SCR-HPC-900 achieves higher ionic diffusion coefficients (D, Table S10, Supporting Information) in both electrolytes, owing to its well-developed conductive network and hierarchical porous structure, which effectively shorten ion diffusion distances and enhance ion migration.

The specific capacitances of the SCR-HPC-900//SCR-HPC-900 symmetric supercapacitors were 52.6, 51.7, 48.5, 46.3, 40.6, and 37.1 F g^{-1} from 0.5 to 50.0 A g^{-1}, respectively (Figure S15b, Supporting Information). Although the specific capacitance in 1 M $TEABF_4$/PC is lower than that in 6 M KOH, the symmetric supercapacitor achieves higher energy density (45.6 Wh kg^{-1}) and power density (41 750 W kg^{-1}) in the organic electrolyte.

This improvement results from a wider voltage window and a dense electric double layer formed in meso-/macropores.[78] In comparison to organic supercapacitors constructed with porous carbons reported in other works, the SCR-HPC-900//SCR-HPC-900 supercapacitor exhibits even more outstanding energy–power integration performance (Table S11, Supporting Information).[17,19,35,42,48] Furthermore, the capacitance retention of 88.5% can be achieved after 100 000 cycles, demonstrating exceptional cycling stability.

3. Conclusion

This study demonstrates a simple and efficient "win-win" strategy for converting Sargentodoxa Cuneata residue (SCR) into hierarchical porous graphitic carbon. Structural characterizations indicate that the decoction pretreatment can effectively modulate the microstructure and chemical composition of raw SC and construct a hierarchical porous architecture rich in active functional groups in biochar, providing abundant active sites and exposed interfaces for the subsequent activation process, which is conducive to the promotion of graphitization of carbon materials while maintaining a high porosity. The optimized SCR-HPC-900 exhibits a high SSA (2465.1 m^2 g^{-1}), a hierarchical porous structure (V_{Tol} of 1.27 cm^3 g^{-1}), as well as a significant degree of graphitization (I_D/I_G of 0.73 and I_{2D}/I_G of 0.50). The SCR-HPC-900 electrode exhibits a high specific capacitance of 415.6 F g^{-1} at 0.5 A g^{-1} in a three-electrode system with 6 M KOH. Impressively, it remains at 312.0 F g^{-1} (75.1%) even at an ultra-high current density of 200 A g^{-1}. The fabricated symmetric supercapacitor achieves an energy density of 8.5 Wh kg^{-1} at a high power density of 37 803 W kg^{-1} and a capacitance retention of 100.8% after 100 000 cycles, demonstrating excellent rate performance and cycling stability. Additionally, the assembled supercapacitors in organic electrolytes obtain the maximum energy density and power density of 45.6 Wh kg^{-1} and 41 750 W kg^{-1}, respectively. This study develops a strategy based on precursor structural engineering, revealing the intrinsic synergistic mechanism between the porous structure development and graphitization enhancement in carbon materials, offering new insights for the development of high-performance carbon materials.

4. Experimental Section

Materials: Sargentodoxa Cuneata (SC) for the experiment was collected from Qiandongnan Prefecture, Guizhou Province, China. Potassium hydroxide (KOH) and hydrochloric acid (HCl) were purchased from Aladdin Life Science Technology Co., Ltd., Shanghai, China. All chemicals were used without further purification.

Synthesis of SCR-HPCs/SC-HPCs: Fresh SC was cut into pieces (~10 cm), washed thoroughly with deionized (DI) water, and then dried at 105 °C for 24 h.

SCR-HPCs were synthesized via a combined carbonization and chemical activation strategy. Specifically, 50 g of dried SC was immersed in a ceramic pot reactor with DI water and decocted at 100 °C for 1 h under atmospheric pressure, with periodic water replenishment to ensure complete submersion. Subsequently, the residue was washed and filtered with DI water, then dried at 105 °C for 24 h to obtain SCR. Next, the dried SCR was placed in a horizontal tube furnace and heated to 700 °C at 5 °C min^{-1} under a nitrogen atmosphere for pyrolytic carbonization for 3 h. After carbonization, the material was naturally cooled, repeatedly washed with 1 M HCl and DI water, and finally dried at 80 °C for 12 h to yield Sargentodoxa Cuneata residue-derived biochar (SCR-BC).

The pre-carbonized SCR-BC was mixed with KOH at a mass ratio of 1:2 and then heated to 800, 900, and 1000 °C, respectively, at a ramp rate of 5 °C min^{-1} in the same tube furnace device and held for 3 h for activation. Finally, the resulting porous carbon samples were thoroughly washed and filtered with 20 wt.% hydrochloric acid (HCl) solution and DI water to remove impurities, then dried at 80 °C for 24 h. The dried samples were subjected to physicochemical characterization and labeled SCR-HPC-X (where X denotes the activation temperature).

As controls, parallel experiments using raw Sargentodoxa Cuneata (SC) without decoction pretreatment were conducted under identical conditions, with products designated as SC-HPC-X. This comparative design enables systematic evaluation of the structural modifications induced by decoction on porous carbon properties.

© 2025 The Author(s). *Energy & Environmental Materials* published by John Wiley & Sons Australia, Ltd on behalf of Zhengzhou University.

Material characterization and electrochemical measurement are provided in the Supporting Information.

Acknowledgements

This research was supported by the Hubei Natural Science Foundation (2022CFC012).

Conflict of Interest

The authors declare no conflicts of interest.

Supporting Information

Supporting Information is available from the Wiley Online Library or from the author.

Keywords

biomass, high rate performance, KOH activation, porous graphitic carbon, supercapacitors

Received: June 19, 2025
Revised: September 4, 2025
Published online: September 8, 2025

[1] P. Simon, Y. GoGotSi, *Nat. Mater.* **2008**, *7*, 845.
[2] L. L. Zhang, X. S. Zhao, *Chem. Soc. Rev.* **2009**, *38*, 2520.
[3] X. Chen, R. Paul, L. Dai, *Natl. Sci. Rev.* **2017**, *4*, 453.
[4] K. Dissanayake, D. Kularatna-Abeywardana, *J Energy Storage* **2024**, *96*, 112563.
[5] D. Khalafallah, Y. Zhang, Q. Zhang, *Batter. Supercaps* **2024**, *8*, e202400497.
[6] X. Liu, D. Lyu, C. Merlet, M. J. A. Leesmith, X. Hua, Z. Xu, C. P. Grey, A. C. Forse, *Science* **2024**, *384*, 321.
[7] A. González, E. Goikolea, J. A. Barrena, R. Mysyk, *Renew. Sust. Energ. Rev.* **2016**, *58*, 1189.
[8] W. Tian, H. Zhang, X. Duan, H. Sun, G. Shao, S. Wang, *Adv. Funct. Mater.* **2020**, *30*, 1909265.
[9] P. Han, M. Cheng, D. Luo, W. Cui, H. Liu, J. Du, M. Wang, Y. Zhao, L. Chen, C. Zhu, J. Xu, *Energy Storage Mater* **2020**, *24*, 486.
[10] Y. Xie, C. Yu, W. Guo, L. Ni, Z. Wang, J. Yu, L. Yang, R. Fu, K. Liu, J. Qiu, *Nano Res* **2021**, *15*, 1399.
[11] D. Khalafallah, D. E. E. Refaay, X. Gu, A. M. A. Henaish, Q. Zhang, *Energy Storage Mater* **2025**, *78*, 104284.
[12] X. Zhang, R. Han, Y. Liu, H. Li, W. Shi, X. Yan, X. Zhao, Y. Li, B. Liu, *Chem. Eng. J.* **2023**, *460*, 141607.
[13] S. Zhang, M. Zheng, Y. Tang, R. Zang, X. Zhang, X. Huang, Y. Chen, Y. Yamauchi, S. Kaskel, H. Pang, *Adv. Funct. Mater.* **2022**, *32*, 2204714.
[14] Y. Li, L. Ni, J. Luo, L. Zhu, X. Zhang, H. Li, I. Zada, J. Yu, S. Zhu, K. Lian, Y. Li, D. Zhang, *Adv. Funct. Mater.* **2024**, *34*, 2403448.
[15] D. Wu, J. Cheng, T. Wang, P. Liu, L. Yang, D. Jia, *ACS Sustain. Chem. Eng.* **2019**, *7*, 12138.
[16] J. Sun, J. Niu, M. Liu, J. Ji, M. Dou, F. Wang, *Appl. Surf. Sci.* **2018**, *427*, 807.
[17] H. Wu, W. Yuan, X. Yuan, L. Cheng, *Energy Storage Mater* **2022**, *50*, 514.
[18] G. Xia, Z. Liu, J. He, M. Huang, L. Zhao, J. Zou, Y. Lei, Q. Yang, Y. Liu, D. Tian, F. Shen, *Renew. Energy* **2024**, *227*, 120478.
[19] K. Nanaji, B. V. Sarada, U. V. Varadaraju, T. N. Rao, S. Anandan, *Renew. Energy* **2021**, *172*, 502.
[20] J. Li, Z. Zhang, Z. Wang, Q. Cao, F. Guo, Q. Cao, *Diam. Relat. Mater.* **2022**, *123*, 108862.
[21] Y. Gong, D. Li, C. Luo, Q. Fu, C. Pan, *Green Chem.* **2017**, *19*, 4132.
[22] Y. Wang, B. Zhang, S. Liu, E. Xu, Z. Wang, *J. Ethnopharmacol.* **2024**, *319*, 117373.
[23] Q. Zhang, L. Lin, W. Ye, *Chin. Med.* **2018**, *13*(1), 1.
[24] C. Bitwell, S. S. Indra, C. Luke, M. K. Kakoma, *Sci. Afr.* **2023**, *19*, e01585.
[25] S. P. S. Chundawat, G. T. Beckham, M. E. Himmel, B. E. Dale, *Annu. Rev. Chem. Biomol. Eng.* **2011**, *2*, 121.
[26] K. Fan, X. Lei, J. Zhang, T. Yu, H. Chen, J. Liu, *Energ. Technol.* **2023**, *11*, 2201281.
[27] H. Zhou, Y. Jing, Y. Wang, *Acta Phys. -Chim. Sin.* **2022**, *40*, 129.
[28] W. Chen, M. Gong, K. Li, M. Xia, Z. Chen, H. Xiao, Y. Fang, Y. Chen, H. Yang, H. Chen, *Appl. Energy* **2020**, *278*, 115730.
[29] A. R. Ferdous, S. S. Shah, S. N. A. Shah, B. A. Johan, M. A. Al Bari, M. A. Aziz, *Molecules* **2024**, *29*, 2081.
[30] J. Zhang, H. Chen, J. Bai, M. Xu, C. Luo, L. Yang, L. Bai, D. Wei, W. Wang, H. Yang, *J. Alloys Compd.* **2021**, *854*, 157207.
[31] Q. Wu, G. Zhang, M. Gao, L. Huang, L. Li, S. Liu, C. Xie, Y. Zhang, S. Yu, *J. Alloys Compd.* **2019**, *786*, 826.
[32] X. Gong, S. Feng, L. Wang, D. Jia, N. Guo, M. Xu, L. Ai, Q. Ma, Q. Zhang, Z. Wang, *Desalination* **2023**, *564*, 116766.
[33] J. Gao, Y. Wang, H. Wu, X. Liu, L. Wang, Q. Yu, A. Li, H. Wang, C. Song, Z. Gao, M. Peng, M. Zhang, N. Ma, J. Wang, W. Zhou, G. Wang, Z. Yin, D. Ma, *Angew. Chem. Int. Ed.* **2019**, *58*, 15089.
[34] H. Liu, S. Zhu, Y. Zhang, H. Song, Y. Zhang, Y. Chang, W. Hou, G. Han, *Small* **2023**, *19*, 2204119.
[35] B. Zhang, F. Sun, Y. Li, D. Wu, C. Yang, Z. Wang, J. Gao, G. Zhao, S. Sun, *Carbon* **2024**, *219*, 118812.
[36] D. Khalafallah, Y. Zhang, H. Dai, C. Liu, Q. Zhang, *Carbon* **2024**, *227*, 119250.
[37] D. Khalafallah, Q. Zhang, *Nano Mater. Sci.* **2025**, *1*, 2.
[38] D. Khalafallah, N. Ibrahim, L. Mohammed, Q. Zhang, *Carbon* **2025**, *231*, 119683.
[39] A. Sadezky, H. Muckenhuber, H. Grothe, R. Niessner, U. Pöschl, *Carbon* **2005**, *43*, 1731.
[40] X. Yao, Y. Ke, W. Ren, X. Wang, F. Xiong, W. Yang, M. Qin, Q. Li, L. Mai, *Adv. Energy Mater.* **2018**, *9*, 1803260.
[41] R. Guo, C. Lv, W. Xu, J. Sun, Y. Zhu, X. Yang, J. Li, J. Sun, L. Zhang, D. Yang, *Adv. Energy Mater.* **2020**, *10*, 1903652.
[42] Y. Lu, G. Zhou, Z. Zhang, C. Li, Q. Dong, Y. Su, W. Chen, *Chem. Eng. J.* **2025**, *508*, 161085.
[43] L. Wang, Q. Zhang, X. Yao, J. Bai, T. Zhou, C. Dong, J. Wu, Y. Zhang, *J. Power Sources* **2025**, *630*, 236079.
[44] J. Mu, Q. Li, X. Kong, X. Wu, J. Sunarso, Y. Zhao, J. Zhou, S. Zhuo, *ChemElectroChem* **2019**, *6*, 4022.
[45] P. Hao, Z. Zhao, Y. Leng, J. Tian, Y. Sang, R. I. Boughton, C. P. Wong, H. Liu, B. Yang, *Nano Energy* **2015**, *15*, 9.
[46] Q. Zhou, H. Li, B. Jia, Y. Dang, G. Zhang, *J. Anal. Appl. Pyrolysis* **2023**, *170*, 105894.
[47] K. Li, Z. Liu, X. Ma, Q. Feng, D. Wang, D. Ma, *New J. Chem.* **2023**, *47*, 5316.
[48] B. Chang, H. Yin, X. Zhang, S. Zhang, B. Yang, *Chem. Eng. J.* **2017**, *312*, 191.
[49] Y. Gong, D. Li, Q. Fu, Y. Zhang, C. Pan, *ACS Appl Energy Mater* **2020**, *3*, 1585.
[50] L. Hou, Z. Chen, Z. Zhao, X. Sun, J. Zhang, C. Yuan, *ACS Appl Energy Mater* **2018**, *2*, 548.
[51] W. Tian, P. Ren, X. Hou, Z. Guo, R. Xue, Z. Chen, Y. Jin, *Ind. Crop. Prod.* **2023**, *202*, 117032.
[52] J. Zhang, J. Luo, Z. Guo, Z. Liu, C. Duan, S. Dou, Q. Yuan, P. Liu, K. Ji, C. Zeng, J. Xu, W. D. Liu, Y. Chen, W. Hu, *Adv. Energy Mater.* **2022**, *13*, 2203061.

© 2025 The Author(s). *Energy & Environmental Materials* published by John Wiley & Sons Australia, Ltd on behalf of Zhengzhou University.

[53] H. Li, Y. Li, Y. Li, H. Shen, S. Zhu, Y. Zhu, K. Lian, *J Energy Storage* **2024**, *77*, 110000.
[54] Y. Wang, X. Dong, Y. Xia, W. Wang, X. Wang, Y. Liu, P. Qiao, G. Zhang, S. Liu, *J. Phys. Chem. Solids* **2025**, *198*, 112472.
[55] J. Dai, G. Li, Y. Hu, L. Han, *J Energy Storage* **2024**, *83*, 110640.
[56] Y. Niu, M. Guo, Y. Zhang, J. Yang, X. Zhang, Y. Gao, X. Wang, L. Sheng, J. Shi, *J Energy Storage* **2023**, *73*, 109064.
[57] Y. Zhang, Z. Yu, W. Yue, X. Zhang, T. He, X. Ma, *J. Ind. Eng. Chem.* **2025**, *142*, 368.
[58] P. Zhang, Y. Li, J. Xiao, W. Ouyang, L. Zhang, D. zhang, G. Wang, L. Liu, Y. Zuo, C. Wang, C. Chen, Y. Zhao, *J. Colloid Interface Sci.* **2025**, *683*, 221.
[59] Y. Li, J. Mei, L. Wu, Q. Xu, Z. Li, *Int. J. Hydrog. Energy* **2024**, *49*, 67.
[60] J. Li, Z. Xia, X. Wang, C. Feng, Q. Zhang, X. a. Chen, Y. Yang, S. Wang, H. Jin, *Adv. Mater.* **2023**, *36*, 2310422.
[61] B. J. Choudhury, H. H. Muigai, P. Kalita, V. S. Moholkar, *Appl. Surf. Sci.* **2022**, *601*, 154202.
[62] W. Yue, Z. Yu, X. Zhang, H. Liu, J. Li, Y. Zhang, X. Ma, *Appl. Surf. Sci.* **2025**, *685*, 162100.
[63] C. Zhao, Y. Ding, Y. Huang, N. Li, Y. Hu, C. Zhao, *Appl. Surf. Sci.* **2021**, *555*, 149726.
[64] J. Wang, Y. Xu, M. Yan, B. Ren, X. Dong, J. Miao, L. Zhang, X. Zhao, Z. Liu, *Biomass Bioenergy* **2022**, *156*, 106301.
[65] T. Wang, Z. Liu, P. Li, H. Wei, K. Wei, X. Chen, *Chem. Eng. J.* **2023**, *466*, 143118.
[66] H. Liu, Y. Wang, L. Lv, X. Liu, Z. Wang, J. Liu, *Energy* **2023**, *269*, 126707.
[67] C. Liu, R. Yuan, Y. Yuan, R. Hou, Y. Liu, W. Ao, J. Qu, M. Yu, H. Song, J. Dai, *Fuel* **2023**, *344*, 128039.
[68] J. Cheng, S. Chen, D. Chen, L. Dong, J. Wang, T. Zhang, T. Jiao, B. Liu, H. Wang, J.-J. Kai, D. Zhang, G. Zheng, L. Zhi, F. Kang, W. Zhang, *J Mater Chem A* **2018**, *6*, 20254.
[69] W. Zhang, B. Zhao, Y. Yin, T. Yin, J. Cheng, K. Zhan, Y. Yan, J. Yang, J. Li, *J Mater Chem A* **2016**, *4*, 19026.
[70] R. Chen, H. Tang, P. He, W. Zhang, Y. Dai, W. Zong, F. Guo, G. He, X. Wang, *Adv. Funct. Mater.* **2022**, *33*, 2212078.
[71] W. Yang, P. Wang, Z. Tu, L. Hou, L. Yan, B. Jiang, C. Zhang, G. Huang, F. Yang, Y. Li, *Carbon* **2022**, *187*, 338.
[72] D. Khalafallah, Q. Zhang, *J Energy Storage* **2024**, *95*, 112621.
[73] B. Ranjan, D. Kaur, Small. **2023**, *20*, 2307723.
[74] J. Cheng, B. Zhao, W. Zhang, F. Shi, G. Zheng, D. Zhang, J. Yang, *Adv. Funct. Mater.* **2015**, *25*, 7381.
[75] D. Khalafallah, M. A. Ibrahim, H. Hou, J. Wang, C. Liu, Q. Zhang, *Sustain. Mater. Technol.* **2025**, *43*, e01286.
[76] H. Liu, W. Shi, H. Song, Y. Chang, L. Feng, W. Hou, Y. Li, Y. Zhao, S. Zhu, G. Han, *ACS Appl Energy Mater* **2022**, *6*, 222.
[77] D. Khalafallah, N. Ibrahim, W. Cao, D. Song, J. Wang, Q. Zhang, *J Energy Storage* **2025**, *110*, 115343.
[78] G. Feng, J. Huang, B. G. Sumpter, V. Meunier, R. Qiao, *Phys. Chem. Chem. Phys.* **2010**, *12*, 5468.

© 2025 The Author(s). *Energy & Environmental Materials* published by John Wiley & Sons Australia, Ltd on behalf of Zhengzhou University.